JOINT INSTITUTE FOR NUCLEAR RESEARCH
Dzhelepov Laboratory of Nuclear Problems

FINAL REPORT ON THE START PROGRAMME

Machine learning methods to separate substances in multi-energy computed tomography based on detectors of the Medipix3RX family

Supervisor:
Vladislav Rozhkov

Student:
Aliaksandr Miadzvetski,
Belarus
Belarusian State University

Participation period:
September 25 – November 06,
Summer Session 2022

Dubna, 2022

Abstract

In computed tomography, materials with different elemental compositions can be represented by the same Hounsfield units, which depend on the mass density of the material. Thus, differentiating and classifying different tissue types and contrast agents can be extremely challenging. In this work, was investigate the possibility of applying machine learning methods to the task of automatically contouring areas containing contrast agents, as well as to the task of differentiating and identifying contrast objects. The data were a series of tomographic images acquired using Medipix 3RX pixelated semiconductor detectors.

Acknowledgments

I want to thank my supervisor Vladislav Rozhkov for project management and his great help in its implementation. Special thanks to the organizing committee for their support and the opportunity to participate in the program. It was a wonderful opportunity to work on an interesting project and get a unique practical experience.

INTRODUCTION

Among all existing imaging techniques, radiation (X-ray) computed tomography (CT) has been particularly successful. CT is based on the ability of X-rays to penetrate matter. It is a powerful tool for examining internal parts of objects without the need for invasive intervention. Until recently, x-ray detectors were only able to measure one scalar quantity: the intensity of the radiation. This led to the emergence of grayscale radiographs. Despite its simplicity, this approach led to the development of sophisticated imaging techniques used today. Among them is computed tomography, which produces three-dimensional X-ray images of objects reconstructed from a set of two-dimensional images taken with a tomograph.

Because the absorption properties of matter are highly dependent on the energy of the radiation, the spectrum of X-rays passing through the object is distorted. In general, low energy photons are absorbed more strongly than high energy photons, and the average energy of the spectrum shifts toward higher values. This effect is called beam hardening. If monochromatic light sources were used in X-ray imaging systems, this effect would not occur. However, at the moment, the only sources capable of emitting monochromatic X-ray beams are large and expensive synchrotrons. In contrast, most imaging applications use X-ray vacuum tubes, which are characterized by emitting a continuum energy spectrum. Although filtering techniques can be applied, the spectra of the tubes always remain polychromatic. As a consequence, when radiographs are made based only on intensity measurements, image artifacts appear. In computed tomography, the effects of beam hardening in two-dimensional images extend to three-dimensional reconstruction, resulting in artifacts that can seriously degrade image quality.

With the development of new detector systems, such as the Medipix readout chip for solid-state pixel sensors, spectral information can be recorded. This information, combined with the high spatial resolution of these detectors, can be used to reduce beam-hardening effects and achieve material decomposition in X-ray computed tomography. Because different colors can be associated with different materials that are recognized, spectral computed tomography is often referred to as color computed tomography.

However, in mono-energy CT imaging, materials with different elemental compositions can be represented by the same or very similar Hounsfield units, which makes differentiating and classifying different tissue types extremely difficult. A classic example is the difficulty in differentiating between calcified plaques and iodine-containing blood. Although these materials differ significantly in atomic number, depending on the corresponding [1].

One option for solving this problem is the use of multi-energy computed tomography. This method uses a series of images taken at different energies to determine the difference in the ability of different materials to absorb X-rays

at different energies. Based on these differences, it becomes possible to differentiate between materials.

This paper investigates the possibility of applying machine learning methods for automatic classification of materials based on data obtained from a multi-energy tomograph.

Chapter 1 gives a general overview of computed tomography and presents the basic image reconstruction methods used to construct a three-dimensional image of a sample from a set of two-dimensional radiographs taken from different angles.

Chapter 2 describes the principles of the Medipix chips, the main differences between several versions of the chips, and a brief description of the properties that characterize their operation.

Chapter 3 discusses the background of multi-energy CT and the algorithm for material decomposition using multi-energy CT.

Chapter 4 presents basic information about machine learning algorithms, as well as the results of applying these methods to the problem of material decomposition.

CHAPTER 1. INTRODUCTION TO COMPUTED TOMOGRAPHY

Computed tomography (CT) scanning is a diagnostic imaging procedure that uses x-rays to build cross-sectional images ("slices") of the body. Cross-sections are reconstructed from measurements of attenuation coefficients of x-ray beams in the volume of the object studied [1].

The detectors of the CT scanner measure the transmission of the X-ray beam through a full scan of the body. The image of that section is taken from different angles, and this allows to retrieve the information on the depth (in the third dimension). The appearance of the scanner in Figure 2.

Figure 2: CT scanner.

The CT scanner is made up of three primary systems, including the gantry, the computer, and the operating console. Each of these is composed of various sub-components. The gantry assembly is the largest of these

systems. It is made up of all the equipment related to the patient, including the patient support, the positioning couch, the mechanical supports, and the scanner housing. It also contains the heart of the CT scanner, the X-ray tube, as well as detectors that generate and detect X-rays.

CHAPTER 2. MEDIPIX SYSTEM DETECTORS

Timepix was conceived as a timing measurement chip with an added functionality of measuring time-over-threshold (ToT). ToT functionality was found useful in many applications, and Timepix3 extends the functionality of Timepix by allowing simultaneous time-of-arrival (ToA)/ToT measurement. It also aims to improve the timing resolution of Timepix. The pixel size has been retained at 55×55μm^2. The Timepix3 engineering run has been funded by Medipix3 collaboration, and it has been a multi-site project between the European Organization for Nuclear Science (CERN) [2,3].

Although full scale (non-prototype) chips with capabilities of simultaneous ToA/ToT measurement do exist, their spatial or timing resolution are not satisfactory for all applications. For example, in it is pointed out, that longitudinal resolution in gas-electron multiplier time projection chambers (GEM-TPCs) could be improved by having better timing resolution in the readout chip. Timepix3 has been designed to address these issues by using pixels of 55μm^2×55μm^2, and as mentioned, by improving timing resolution. The timing improvement has been achieved by using voltage-controlled oscillators (VCOs) inside the pixel matrix. In some low duty cycle applications power consumption needs to be reduced by additional means. An on-chip power pulsing functionality has been added into Timepix3 to support its deployment in these applications. Main usage of Timepix3 is seen to being particle tracking applications where timing and spatial resolution are important. However, the chip can be programmed in event counting or photon counting mode and used in imaging applications with higher particle rates than 40Mhits/cm^2/s. The choice of the sensor will depend on the particular application but the first assemblies with a bonded sensor will use silicon sensors. In GEM-TPCs Timepix3 will be used without any sensor on top [2,3].

CHAPTER 3. MULTI-ENERGY COMPUTED TOMOGRAPHY

In x-ray computed tomography (CT), materials having different elemental compositions can be represented by identical pixel values on a CT image (ie, CT numbers), depending on the mass density of the material. Thus, the differentiation and classification of different tissue types and contrast agents can be extremely challenging. In dual-energy CT, an additional attenuation measurement is obtained with a second x-ray spectrum (ie, a second “energy”), allowing the differentiation of multiple materials. Alternatively, this allows quantification of the mass density of two or three materials in a mixture with known elemental composition. Recent advances in

the use of energy-resolving, photon-counting detectors for CT imaging suggest the ability to acquire data in multiple energy bins, which is expected to further improve the signal-to-noise ratio for material-specific imaging [4].

CHAPTER 4. APPLICATION OF MACHINE LEARNING METHODS IN THE PROBLEM OF CONTRAST SEPARATION

4.1 Using OpenCV for automatic contouring of region of interest (RoI)

The reconstruction of a 3D tomographic image results in a set of layer-by-layer images. The image is a tiff file, each pixel of which stores the value of material absorption coefficient.

In the current work, tomographic images of a Plexiglas phantom containing samples with different types of contrast and at different concentrations were investigated. A picture of the phantom with signed objects is shown in Figure 4.1.

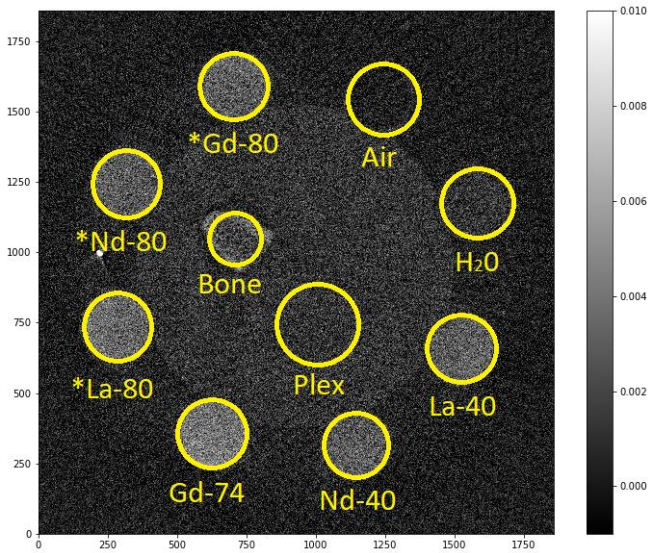

Figure 4.1: Tomographic image of the phantom.

To create Figure 4.1, the center of the circle was defined manually. After that, the circle containing the RoI was constructed using the Python. Selection of the RoI is necessary for further analysis, which will be described in the following paragraphs.

However, this task can be automated using computer vision techniques. Since the RoI can be described by a primitive shape, the Hough transform can be used to find primitives in the image.

The Hough transform is based on the representation of the object being sought in the form of a parametric equation. The parameters of this equation represent the phase space (the so-called accumulator array/space, Hough space). Then, a binary image is taken. All the boundary points are tried and the assumption is made that the point belongs to the line of the object sought

thus, for each image point, the desired equation is calculated and the necessary parameters are obtained, which are stored in Hough space. The final step is to bypass the Hough space and select the maximum values for which the most pixels in the picture "voted", which gives us the parameters for the equations of the sought object.

The following algorithm is used to find circles using the Hough transform:

1. uses the Kenny boundary detector to find boundaries in the image;
2. the gradient is calculated for non-zero points (by calculating the 1st derivative on X and Y through cvSobel());
3. the centers of the circles are determined;
4. the non-zero points lying at the same distance are defined with respect to the center.

In OpenCV, the Hough transform for finding circles is implemented by the cvHoughCircles() function. The standard parameters of the cvHoughCircles() function are shown in Figure 4.2:

```
1.  CVAPI(CvSeq*) cvHoughCircles( CvArr* image, void* circle_storage,
2.                                int method, double dp, double min_dist,
3.                                double param1 CV_DEFAULT(100),
4.                                double param2 CV_DEFAULT(100),
5.                                int min_radius CV_DEFAULT(0),
6.                                int max_radius CV_DEFAULT(0));
```

Figure 4.2: Standard parameters of the cvHoughCircles() function.

After finding the coordinates of the centers of the circles using cvHoughCircles(), they were constructed using Python. The results are shown in Figure 4.3.

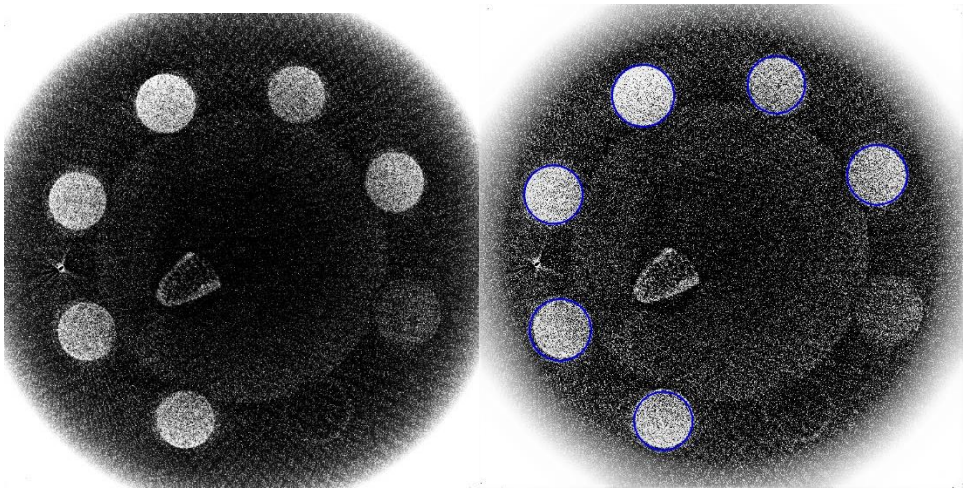

(а) (б)

Figure 4.3: Automatic RoI extraction

Figure 4.3 shows that the algorithm was able to select six RoIs out of eight (in this work only tubes with contrasting substance were selected and samples with Plexiglas, air and bone were not considered). The remaining two RoIs remained unselected, most likely due to the fact that they have

poorly distinguishable boundaries and the Hough transform cannot distinguish them.

4.2 Preparing Data Sets for Applying Machine Learning Algorithms

Tomographic images obtained at different threshold values (approximate energies between 20 and 80 KeV) were used in the work.

After the RoI was detected, the pixel values contained in it were averaged, after which the value was recorded in a column named thl value. An additional column containing the class label (material or K-edge value) was also created.

Cubic interpolation was used to recover missing values. The final data set for material prediction took the form of the table shown in Figure 4.4.

	material	thl45	thl46	thl47	thl48	thl49	thl50	thl51	thl52	thl53	...	thl156	thl157	thl158	thl159	thl160
0	La	0.002733	0.002730	0.002726	0.002723	0.002719	0.002716	0.002713	0.002710	0.002708	...	0.001535	0.001519	0.001503	0.001488	0.001473
1	La	0.002976	0.002931	0.002891	0.002856	0.002825	0.002798	0.002776	0.002757	0.002741	...	0.001543	0.001526	0.001510	0.001494	0.001478
2	La	0.002956	0.002916	0.002881	0.002851	0.002824	0.002802	0.002783	0.002768	0.002755	...	0.001463	0.001446	0.001431	0.001417	0.001406
3	La	0.002952	0.002913	0.002879	0.002848	0.002820	0.002795	0.002773	0.002754	0.002737	...	0.001508	0.001491	0.001476	0.001461	0.001448
4	La	0.002986	0.002939	0.002897	0.002860	0.002828	0.002801	0.002777	0.002758	0.002742	...	0.001480	0.001463	0.001446	0.001431	0.001417
...	...	...	...	...	...	...	...	...	...	...	...	...	...	...	...	...
79483	water	0.001881	0.001732	0.001604	0.001494	0.001402	0.001327	0.001267	0.001220	0.001185	...	0.000792	0.000788	0.000783	0.000775	0.000765
79484	water	0.001920	0.001781	0.001660	0.001558	0.001471	0.001400	0.001342	0.001297	0.001263	...	0.000605	0.000602	0.000600	0.000601	0.000603
79485	water	0.001826	0.001715	0.001616	0.001528	0.001452	0.001387	0.001330	0.001283	0.001244	...	0.000665	0.000664	0.000664	0.000664	0.000666
79486	water	0.001187	0.001187	0.001187	0.001186	0.001184	0.001182	0.001179	0.001175	0.001171	...	0.000660	0.000658	0.000656	0.000653	0.000650
79487	water	0.001860	0.001739	0.001633	0.001540	0.001459	0.001390	0.001332	0.001283	0.001243	...	0.000722	0.000719	0.000715	0.000710	0.000704

79488 rows × 122 columns

Figure 4.4: Prediction dataset

Also, before using machine learning algorithms, the data set was partitioned into a training sample and a test sample (the test sample was 33% of the total number of rows), using the train_test_split() function from the scikit-learn library.

4.3 Gradient Boosting for Material Recognition

Material recognition is a classification task with 6 classes: La, Nd, Gd, water, air and Plexiglas. It was decided to use gradient boosting from the Xgboost library to create a classifier. Selected parameters of the classifier based on gradient binning are shown in Figure 4.5.

```
XGBClassifier(base_score=0.5, booster='gbtree', colsample_bylevel=1,
              colsample_bynode=1, colsample_bytree=1, enable_categorical=False,
              gamma=0, gpu_id=-1, importance_type=None,
              interaction_constraints='', learning_rate=0.300000012,
              max_delta_step=0, max_depth=6, min_child_weight=1, missing=nan,
              monotone_constraints='()', n_estimators=100, n_jobs=4,
              num_parallel_tree=1, objective='multi:softprob', predictor='auto',
              random_state=0, reg_alpha=0, reg_lambda=1, scale_pos_weight=None,
              subsample=1, tree_method='exact', use_label_encoder=True,
              validate_parameters=1, verbosity=None)
```

Figure 4.5: Classifier parameters.

The quality of the predictions was evaluated by the error matrix, the form of this matrix is shown in Figure 4.6.

		Predicted	
		Negative **(N)** **-**	Positive **(P)** **+**
Actual	Negative **-**	True Negative **(TN)**	**False Positive (FP) Type I Error**
	Positive **+**	**False Negative (FN) Type II Error**	True Positive **(TP)**

Figure 4.6: Error matrix.

The results of the evaluation on the test sample are shown in Figure 4.7.

```
[21729     2] [21656     0] [21596     0] [20036     0] [22215     0] [23924     2]
[    0  4501] [    0  4576] [    2  4634] [    0  6196] [    2  4015] [    0  2306]
```

a) La b) Gd c) Nd d) air e) plex f) water

Figure 4.7: Error matrices on the test sample.

As can be seen from Figure 4.7, the number of false positive and false negative cases is very small and the accuracy of the predictions reaches 99%, which is suspicious and requires further research.

4.4 Gradient Boosting for K-edge Prediction

In X-ray absorption spectroscopy, a K-edge is a sudden increase in X-ray absorption that occurs when the energy of the X-ray radiation is just above the binding energy of the innermost electron shell of atoms interacting with photons. Physically, this sudden increase in attenuation is caused by photoelectric absorption of photons. For this interaction to occur, photons must have an energy greater than the binding energy of the K-shell electrons (K-edge). Therefore, a photon with an energy just above the binding energy of an electron is more likely to be absorbed than a photon with an energy just below that binding energy or significantly above it.

After interpolating the missing values, plots were made of the dependence of the ratio value on the energy at which the picture was taken. The graphs are shown in Figure 4.8.

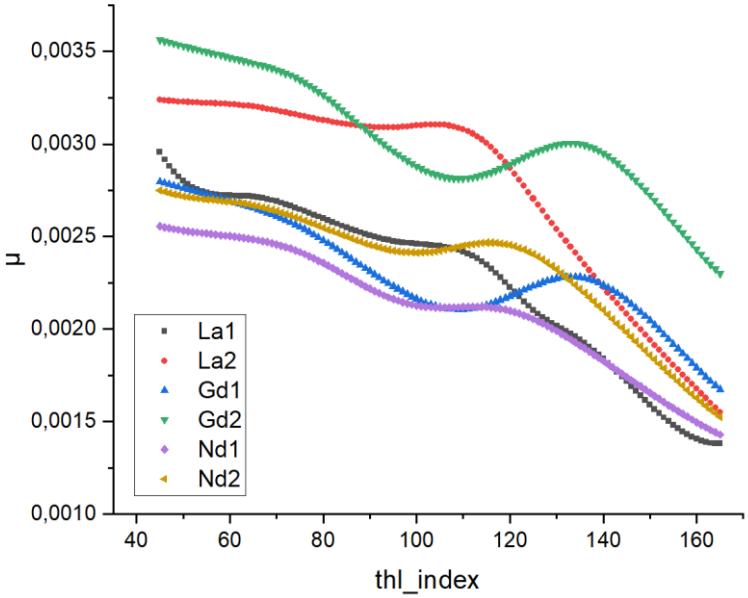

Figure 4.8: Plots of ratio value dependence on energy.

Manually determined values of k-edge for each contrast agent, their values are shown in Table 4.1.

Table 4.1: Value of k-edge for contrast agents.

Contrast agent	K-edge value
La	98
Gd	110
Nd	121

The obtained values were entered into the training dataset.

For automatic determination of the K-edge a regressor based on gradient boosting was used, parameters of the regressor are shown in Figure 4.9.

```
XGBRegressor(base_score=0.5, booster='gbtree', colsample_bylevel=1,
             colsample_bynode=1, colsample_bytree=1, enable_categorical=False,
             gamma=0, gpu_id=-1, importance_type=None,
             interaction_constraints='', learning_rate=0.300000012,
             max_delta_step=0, max_depth=6, min_child_weight=1, missing=nan,
             monotone_constraints='()', n_estimators=10, n_jobs=4,
             num_parallel_tree=1, objective='reg:linear', predictor='auto',
             random_state=123, reg_alpha=0, reg_lambda=1, scale_pos_weight=1,
             seed=123, subsample=1, tree_method='exact', validate_parameters=1,
             verbosity=None)
```

Figure 4.9: Regressor parameters.

The quality assessment was carried out according to the coefficient of determination R^2, as well as the mean absolute error (MAE). MAE was chosen because it is more robust to outliers than the root means square error (MSE).

A bar graph of the range of predicted values was also plotted, shown in Figure 4.10.

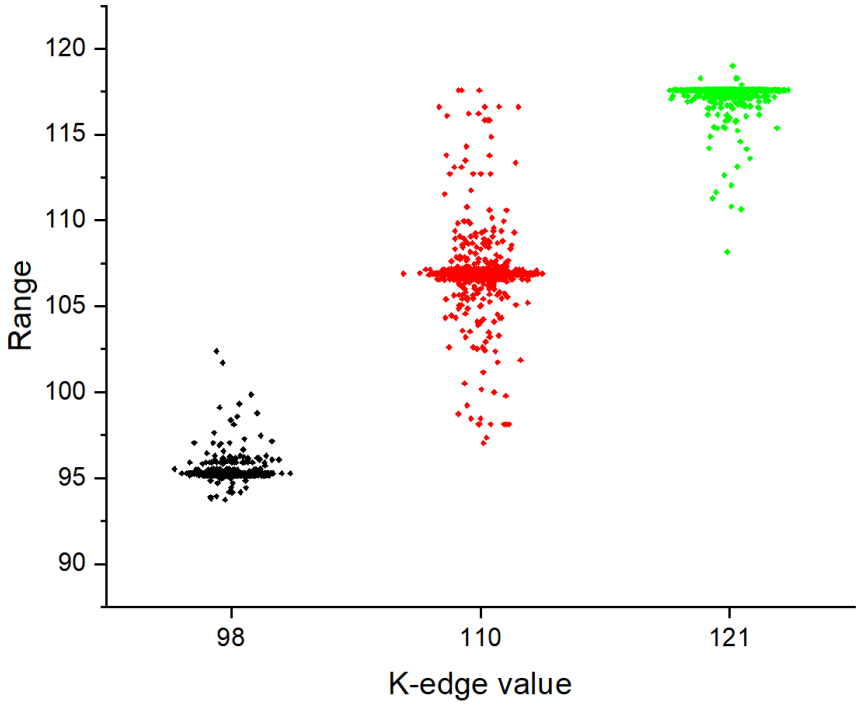

Figure 4.10: Bar graph of the range of predicted values.

Formula 4.1 was used to calculate the MAE:

$$MAE = \frac{1}{N}\sum_{i=1}^{N} y_i - \hat{y}_i \vee \quad (4.1)$$

As a result of the cross-validation calculations, the MAE value was 3.13. The coefficient of determination R^2 is calculated by formula 4.2.

$$R^2 = 1 - \frac{MSE(model)}{MSE(baseline)} \quad (4.2)$$

To use formula 4.2, find the MSE (model) and MSE (baseline) using formulas 4.3 and 4.4, respectively.

$$MSE(model) = \frac{1}{N}\sum_{i=1}^{N}(y_i - \hat{y}_i)^2 \quad (4.3)$$

where y_i is the actual expected result and $\hat{y}_i$ the model prediction.

$$MSE(baseline) = \frac{1}{N}\sum_{i=1}^{N}(y_i - \overline{y_i})^2 \quad (4.4)$$

where $\overline{y} = \frac{1}{n}\sum_{i=1}^{n} y_i$

The R^2 score was 88%, which indicates to good algorithm prediction for the lanthanides recognition.

CONCLUSION

In X-ray computed tomography (CT), materials with different elemental compositions can be represented by the same pixel values in the CT image (i.e., CT numbers), depending on the mass density of the material. Thus, the differentiation and classification of different tissue types and contrast agents can be extremely challenging.

In this work, we investigated the possibility of applying machine learning methods to the task of automatically contouring areas containing contrast agents, as well as to the task of differentiating and identifying contrast objects. The data were a series of tomographic images acquired with Medipix 3RX pixel solid-state detectors.

For automatic contouring of areas, computer vision techniques were applied. With the help of Hough algorithm, six areas out of eight were identified. This result shows the possibility of using these methods to automate the contouring task, but further research and improvements are needed.

To classify different contrast agents, a classifier based on gradient binning was constructed. To assess the quality of the model, tests were conducted on the test sample and an error matrix was constructed, as a result, the accuracy of the model was 98%. In the future, the model is to be tested to search for contrast agents in the image.

A regression model was also built to determine the K-edge of contrast agents. The regressor is also based on gradient boosting. The quality of the model was checked by calculating the mean absolute error (MAE) on cross-validation as well as by using the coefficient of determination R^2. The resulting MAE and R^2 values were 3.13 and 88%, respectively.

The results prove the possibility of using machine learning methods in the tasks of contrast agent differentiation and autocontouring of the areas under study. However, further research and improvement of the available models is required, and other basic algorithms should be considered.

References

1. Buzug T. M. (2011). Computed Tomography, Handbook of Medical Technology, Springer-Verlag, Berlin Heidelberg.

2. Llopart, X., Ballabriga, R., Campbell, M., Tlustos, L., & Wong, W.S. (2007). Timepix, a 65k programmable pixel readout chip for arrival time, energy and/or photon counting measurements. Nuclear Instruments & Methods in Physics Research Section A-accelerators Spectrometers Detectors and Associated Equipment, 581, 485-494.

3. Poikela, T.S., Plosila, J., Westerlund, T., Campbell, M., Gaspari, M.D., Llopart, X., Gromov, V., Kluit, R., Beuzekom, M.V., Zappon, F., Zivkovic, V.A., Brezina, C., Desch, K.K., Fu, Y., & Kruth, A. (2014). Timepix3: a 65K channel hybrid pixel readout chip with simultaneous ToA/ToT and sparse readout. Journal of Instrumentation, 9, C05013 - C05013.

4. McCollough, C.H., Leng, S., Yu, L., & Fletcher, J.G. (2015). Dual- and Multi-Energy CT: Principles, Technical Approaches, and Clinical Applications. Radiology, 276 3, 637-53.